

The flapping-flag instability as a nonlinear eigenvalue problem

Silas Alben^{a)}

School of Mathematics, Georgia Institute of Technology, Atlanta, Georgia 30332-0160, USA

(Received 9 June 2008; accepted 18 September 2008; published online 20 October 2008)

We reconsider the classical problem of the instability of a flapping flag in an inviscid background flow with a vortex sheet wake, and reformulate it as a nonlinear eigenvalue problem. We solve the problem numerically for the 20 lowest wave number modes. We find that the lowest wave number mode is the first to become unstable, and has the fastest growth rate within 3.5 decades of the stability boundary in the parameter space of flag mass and flag rigidity. This and subsequent modes become unstable by merging into complex-conjugate pairs, which then lose conjugacy further into the region of instability. Eigenmodes exhibit sharp transitions in shape across the stability boundary. In the corresponding initial value problem, we show a correlation between the wave number of unstable modes in the small-amplitude (growth) regime and the large-amplitude (saturation) regime. Wave number increases with decreasing rigidity and shows a combination of discrete and continuous change in the shape of unstable modes. Using an infinite flag model we compute the parameters of the most unstable flag and show that a classical mechanism for the instability correlating pressure lows to flag amplitude peaks does not hold. © 2008 American Institute of Physics. [DOI: 10.1063/1.3000670]

I. INTRODUCTION

A classical and fundamental problem in the field of fluid-structure interaction is the flapping-flag instability. Fluid mechanical studies of the phenomenon date back at least to the 19th century,¹ increased in number during the early days of aerodynamics and aeroelasticity,² and have continued to the present with increasingly accurate representations for the coupled fluid-structure interaction.^{3–8}

The problem continues to attract attention because the effect of fluid forces on stability is nonobvious. The linear stability problem for a beam with mass in a vacuum yields neutrally stable modes.⁹ Replacing the vacuum with a fluid environment yields fluid forces on the beam, which can be either stabilizing and destabilizing depending on the control parameters' values and the instantaneous state of the dynamical system.

Simple exact unsteady solutions of flexible bodies in inviscid flows with vorticity are elusive. *Steady* flows, however, provide some physical intuition. In one example, a rigid plate hinged at the leading edge and slightly inclined to a steady flow, the pressure forces are stabilizing. Here the center of pressure lies one-quarter chord behind the leading edge and applies a torque which aligns the plate with the flow. However, in another example, the steady flow past a flexible sheet with a sinusoidal profile, pressure forces are *destabilizing*: pressure minima occur at the peaks and maxima at the troughs, which tend to increase the amplitude of the sine wave. Prandtl¹⁰ considered this pressure jump as a mechanism for the Kelvin–Helmholtz instability of a free vortex sheet (in the absence of a flag). These examples consider steady flows only as a model for the actual unsteady fluid flows, however. Unsteady fluid forces, for example, related

to the growth of vorticity in the wake of the flag, couple to flag dynamics and alter the stability of the system.

Recently, Shelley *et al.*⁵ considered the linear stability of an infinite periodic sheet, for which the solution is a superposition of sinusoidal traveling waves. These are perhaps the simplest known unsteady solutions which couple the fluid forces to the flag motion. Later, Alben and Shelley⁸ considered the stability of a *finite* flag with a free vortex wake to small but finite disturbances. Here the free vortex wake is a source of nonlinearity even for small deflections, and prevents a simple exact solution. In both cases, a nontrivial stability behavior was found with respect to flag mass. In short, smaller flag mass increases the range of rigidity for which the flag is stable. In this work, we formulate and solve the linear stability problem for the finite flag with a free vortex wake. We are able to expand greatly on the stability results of Ref. 8 because the nonlinear eigenvalue problem considered here is much less expensive to solve than the nonlinear initial value problem simulated in Ref. 8. This study is therefore able to present a more complete characterization of the flapping modes and growth rates for the linear instability of a flapping flag.

Previous studies^{11–13} have found good agreement between simulations using the vortex sheet model given here and experiments. These experiments considered unsteady flows past wedges¹² and ejection from a tube orifice,¹¹ at Reynolds numbers in the range of 10^3 – 10^5 . The vortex sheet model neglects the viscous boundary layer. Separation is not expected because the flag is nearly aligned with the free stream. However, the viscous boundary layer could have an effect on stability, as was conjectured in the comparison between experiments and theory of Ref. 5. Here we concern ourselves with stability properties in the simpler inviscid model, which is also a reasonable starting point for a boundary-layer study.

^{a)}Electronic mail: alben@math.gatech.edu.

Section II presents the linearized flag model, the resulting nonlinear eigenvalue problem, and the numerical continuation method used to solve the eigenvalue problem. Section III presents the main results. First, we compute the growth rates (and stability boundary) of the fastest growing mode, in the two-dimensional space of dimensionless flag mass and rigidity. In this region (within 3.5 decades of the stability boundary in both dimensionless parameters), the longest wavelength eigenmode always grows fastest. Also, for each rigidity there is a finite mass at which the instability grows fastest. This mass is not much greater than the threshold mass at which instability begins. We find also that the frequency of oscillation tends to a constant as flag rigidity is decreased. We then study the eigenvalues as the flag becomes unstable. We find that pairs of eigenvalues merge into an approximately conjugate pair (one stable and one unstable) at the stability boundary. However, the conjugacy relationship holds only when the eigenvalues are much less than one, when the eigenvalue problem is well approximated by a linear eigenvalue problem. We compute the boundaries where the first 20 modes become unstable in parameter space, which are described by only five curves. Each curve represents a class of four modes, any two members of which are related by negating the real and/or imaginary parts. Higher wave number modes first become unstable at smaller rigidities than lower modes. We then consider the first two unstable eigenmode *shapes* over a large region of parameter space. The shapes change most rapidly when they are unstable, and here the imaginary part becomes significant, which corresponds to fluid forcing terms.

In Sec. IV we turn to simulations of the initial value problem for one flag mass, $R_1=0.1$, and rigidities R_2 over a factor of 30, moving from the stability boundary into the region of instability. We examine how the flag shape in the small-amplitude regime changes with rigidity. We find a series of plateaus in the first moment of the wave number, which indicates that the flag makes a discrete series of transitions. We then consider the relationship between the flag shape in the small-amplitude regime, and the eventual large-amplitude shapes of the flag. We find that high wave number modes in the linear regime lead to high wave number modes in the large-amplitude regime. Furthermore, irregularity in large-amplitude dynamics appears to set in when three or more modes are unstable in the small-amplitude analysis.

Section V considers the role of two numerical parameters: δ and L_w . The initial value problem simulations of Sec. IV and Ref. 8 require a smoothing of the vortex sheet wake, with parameter δ (a smoothing length scale) we set to 0.2. To measure the effect of δ on stability, we solve the eigenvalue problem with different values of δ , and find that incorporation of δ accounts for most of the difference in stability boundary position between the eigenvalue problem and the initial value problem. Another difference between the problems is that the eigenvalue problem assumes a free vortex wake of a given length L_w , while the initial value problem has a growing vortex wake. We test the dependence of the eigenvalues on L_w , and find the stability boundary changes only modestly, and differences in growth rates are small and decrease as we move into the instability region.

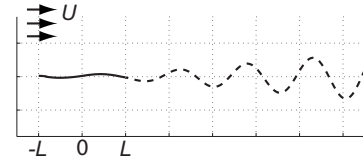


FIG. 1. A schematic of the flapping flag of length $2L$ in a stream of flow speed U .

II. LINEARIZED FLAG MODEL

We present a model for the dynamics of a flexible slender body nearly aligned with an inviscid flow. The body, or flag, obeys the Kutta condition of finite velocity at the trailing edge. Similar models have been derived and studied previously,^{3,8,14} and background elements of the formulation here have been presented previously in Refs. 8 and 15. We therefore focus on the points specific to the model at hand, and to the computation of eigenmodes and eigenfrequencies.

We consider a slender body of length $2L$, nearly aligned with a fluid stream of speed U in the far field (see Fig. 1). In the following equations, we nondimensionalize lengths by L and time by L/U . We consider small deflections $y(x,t)$ linearized about the straight configuration, aligned with the flow. The body behaves as a linear beam under a pressure loading,

$$R_1 \partial_{tt} y = -R_2 \partial_{xxxx} y - [p]. \quad (1)$$

Here $R_1 = \rho_s / \rho_f L$ is the body mass per unit length nondimensionalized by fluid mass per unit area, times body length. The second important dimensionless parameter is $R_2 = B / \rho_f U^2 L^3$, the (spatially uniform) body rigidity B nondimensionalized by fluid inertia. The flag is clamped at the leading edge, and free at the trailing edge (see Ref. 9)

$$y|_{x=-1} = \partial_x y|_{x=-1} = 0, \quad \partial_{xx} y|_{x=1} = \partial_{xxx} y|_{x=1} = 0. \quad (2)$$

The dynamics of flag bending is coupled to the fluid flow through $[p](x,t)$, the difference in pressure from the positive side to the negative side. The positive side is located to the left as one traverses the flag from leading to trailing edge. Using the unsteady Bernoulli equation, $[p]$ may be expressed as (see Ref. 16 or 8; the opposite sign convention is used for $[p]$ here)

$$\partial_t \gamma + \partial_x \gamma = \partial_x [p]. \quad (3)$$

Here γ is the difference across the body of the component of flow velocity tangent to the body: $\gamma = \mathbf{u} \cdot \hat{\mathbf{s}}|_+^-$. Here \mathbf{u} is the flow velocity and $\hat{\mathbf{s}}$ is the local unit tangent vector. Equivalently, γ is the density of a “bound” vortex sheet located on the body. The difference between the average flow speed tangent to the fiber, and the fiber’s own tangential speed, multiplies the term $\partial_x \gamma$ in Eq. (3). This difference is 1 up to linear order in flapping amplitude.

The set of equations is closed by relating $\gamma(x,t)$ back to the body position $y(x,t)$. The relation is the kinematic condition, which states that fluid does not penetrate the body. In the linearized case considered here, the equation has also been called the airfoil equation:²

$$\partial_t y(x,t) + \partial_x y(x,t) = \frac{1}{2\pi} P \int_{-1}^1 \frac{v(x',t) dx'}{\sqrt{1-x'^2}(x-x')} + b(x,t),$$

$$-1 < x < 1. \quad (4)$$

Here v is a bounded function, related to the vortex sheet strength by $\gamma = v/\sqrt{1-x^2}$, which shows the inverse square-root singularities which arise in γ at the flag end points. Such singularities are generic for solutions to Eq. (4) (see Ref. 17).

Here $b(x,t)$ is the velocity induced by the vortex sheet wake, which extends downstream from the flag on the interval $1 < x < L_w$:

$$b(x,t) = \frac{1}{2\pi} \int_1^{L_w} \frac{\gamma(x',t)}{x-x'} dx'. \quad (5)$$

The circulation of the wake,

$$\Gamma(x,t) = \int_x^{L_w} \gamma(x',t) dx', \quad (6)$$

is conserved along material points of the wake, which move according to Birkhoff–Rott equation.¹⁶ Here we are concerned only with small-amplitude motions of the flag, in which case the dynamics of the wake is simply uniform flow at the free-stream speed 1 along the x -axis.

At each time t , the vorticity created at the trailing edge of the flag, or alternatively the total circulation in the wake $\Gamma(1,t)$, is set by the condition that the flow velocity (or γ) be finite at the trailing edge. Equivalently,

$$v(1,t) = 0. \quad (7)$$

Equations (1), (3)–(5), and (7) are the system of equations which we shall use to determine the motion of the flag and the strength of the vortex sheets along the body and in the wake.

We address the stability of the system by searching for solutions in the form

$$y(x,t) = Y(x)e^{i\sigma t}; \quad \gamma(x,t) = g(x)e^{i\sigma t},$$

$$v(x,t) = V(x)e^{i\sigma t}, \quad \Gamma(1,t) = \Gamma_0 e^{i\sigma t}, \quad (8)$$

where Y, g, V , and Γ_0 are eigenmodes with complex eigenfrequencies σ . Unstable eigenmodes are those for which σ has negative imaginary part. We wish to identify the region of R_1 - R_2 space in which unstable eigenmodes exist, and when there are multiple unstable modes, identify the fastest growing mode.

Inserting eigenmode (8) into the equations yields

$$-\sigma^2 R_1 Y = -R_2 \partial_{xxx} Y - i\sigma g - \partial_x g \quad (9)$$

for Eqs. (1) and (3); and for Eq. (4):

$$i\sigma Y + \partial_x Y = \frac{1}{2\pi} P \int_{-1}^1 \frac{V(x') dx'}{\sqrt{1-x'^2}(x-x')} + B(x,\sigma),$$

$$-1 < x < 1. \quad (10)$$

Here $B(x,\sigma)$ is the term corresponding to $b(x,t)$, and takes a particularly simple form, because of the property that values of the circulation $\Gamma(x,t)$ are conserved on material points of

the vortex sheet wake, which move downstream at dimensionless speed 1 (up to linear order in flag flapping amplitude) along the positive x -axis. Thus the material point at location $x \geq 1$ at time t was at location $x=1$ at time $t-(x-1)$. Thus by Eq. (8),

$$\Gamma(x,t) = \Gamma_0 e^{i\sigma(t-(x-1))}, \quad 1 < x < L_w, \quad (11)$$

$$\gamma(x,t) = \partial_t \Gamma(x,t) = -i\sigma \Gamma_0 e^{-i\sigma(x-1)} e^{i\sigma t}, \quad 1 < x < L_w. \quad (12)$$

Thus, $b(x,t)$ in Eq. (5) becomes

$$b(x,t) = -\frac{1}{2\pi} \Omega \Gamma_0 P \int_1^{L_w} \frac{e^{-i\sigma(x'-1)}}{x-x'} dx' e^{i\sigma t} \quad (13)$$

and

$$B(x,\sigma) = -\frac{1}{2\pi} \Omega \Gamma_0 P \int_1^{L_w} \frac{e^{-i\sigma(x'-1)}}{x-x'} dx'. \quad (14)$$

Because σ appears in the exponential in B , we have a nonlinear eigenvalue problem. We solve the problem iteratively, by continuation, starting from the limit that $R_1, R_2 \gg 1$. In this limit we have the linear eigenvalue problem of a cantilever oscillating in a vacuum:

$$-\sigma^2 R_1 Y = -R_2 \partial_{xxx} Y. \quad (15)$$

The eigenmodes are linear combinations of the four terms $\cos kx$, $\sin kx$, $\sinh kx$, and $\cosh kx$; $k = (\sigma^2 R_1 / R_2)^{1/4}$ satisfying the four boundary conditions (2). Nontrivial linear combinations exist for values of k such that the determinant of the matrix

$$\begin{pmatrix} \sin(-k) & \cos(-k) & \sinh(-k) & \cosh(-k) \\ \cos(-k) & -\sin(-k) & \cosh(-k) & \sinh(-k) \\ -\sin(k) & -\cos(k) & \sinh(k) & \cosh(k) \\ -\cos(k) & \sin(k) & \cosh(k) & \sinh(k) \end{pmatrix}$$

vanishes, which occurs for

$$k = 0.9376, 2.3470, 3.9273, 5.4978, \dots \quad (16)$$

Subsequent terms in the k sequence are very nearly $\pi/2$ apart. For each k , there are a pair of eigenfrequencies:

$$\sigma = \pm \sqrt{(R_2/R_1)} k^2. \quad (17)$$

If $R_1, R_2 \gg 1$ but both are finite, the nonlinearity is weak and eigenfrequencies and modes are well approximated by those for the cantilever. We use them as initial guesses in a Newton iteration for the nonlinear eigenvalue problem represented by Eqs. (9) and (10). At each iteration of Newton's method, we have a guess σ_0 for a particular eigenfrequency. Prior to the iteration, we separate terms in the equations by the powers of σ they include, and write the equations as a quadratic eigenvalue problem of the form

$$[\sigma^2 A_2 + \sigma A_1 + A_0(\sigma_0)]w = 0, \quad (18)$$

where w is the vector consisting of (1) values of the eigenmodes (here defined as the values of the beam curvature

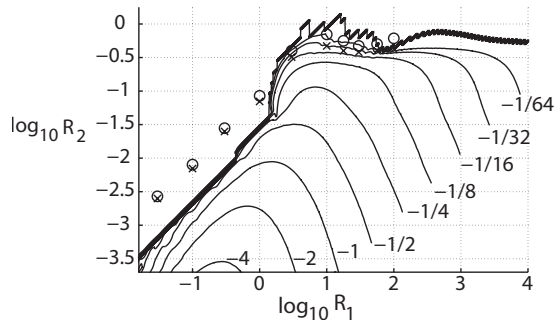


FIG. 2. The region in R_1 - R_2 space in which the flag is linearly unstable. The thick black line marks the location of the linear stability boundary. The vertical resolution of the data is approximately half the size of the jumps in the zigzag line. The horizontal resolution of the data is finer: one data point for every multiplicative change of 1.01 in R_1 . The contours below the stability boundary give the value of the imaginary part of the eigenfrequency corresponding to the most unstable mode. Plotted also are large circles and crosses, which represent the stability boundary computed numerically in Ref. 8.

$\partial_{xx}Y$) on the Chebyshev mesh $\{x_i = \cos \theta_i, \theta_i = i\pi/m, i = 0, \dots, m\}$; and (2) the scalar G_0 .

The “constant” matrix $A_0(\sigma_0)$ is actually a function of σ , because it includes the exponential integral involving σ in Eq. (10). However it is held constant, with σ_0 from the previous Newton iteration, while the quadratic eigenvalue problem (18) is solved using MATLAB. The nearest eigenvalue to σ_0 from the quadratic eigenvalue problem is then substituted for σ_0 , and the process is repeated until one of the eigenfrequencies of the quadratic eigenvalue problem σ equals σ_0 up to a preset tolerance, at which point σ_0 approximates a solution to the nonlinear eigenvalue problem.

In the system of Eq. (18), σ always appears in powers of $i\sigma$. Therefore, all terms involving σ in the system of equations are changed to their complex conjugate when $\sigma_R + i\sigma_I$ is changed to $-\sigma_R + i\sigma_I$, where σ_R and σ_I are the real and imaginary parts, respectively, of σ . Taking the complex conjugate of the eigenvalue equations, we find eigenmodes for the eigenvalues $-\sigma_R + i\sigma_I$ by simply taking the complex conjugate of the eigenmodes for $\sigma_R + i\sigma_I$. Thus we can generate all eigenmodes by computing just one member of the conjugate pair of eigenmodes and corresponding eigenvalues. Of the first ten conjugate pairs of cantilever eigenmodes, we track the member of the pair corresponding to the eigenvalue with positive real part, by continuation as R_1 and R_2 are decreased from $R_1, R_2 \gg 1$.

III. RESULTS

We track by continuation in R_1 and R_2 20 eigenfrequencies, which, when R_1 and R_2 are large, are the lowest 20 frequencies—approximately those of the cantilever problem. In Fig. 2 we plot the region of instability; that is, the region of R_1 - R_2 space in which at least one of the 20 modes has eigenfrequency with negative imaginary part, and is therefore unstable. The stability boundary (zigzag line) is nearly flat at larger R_1 , and linear at smaller R_1 , which agrees with previous linearized^{5,6} and nonlinear studies.⁸ The upper and lower bounds from the latter study are superposed (circles and crosses), and show good agreement at larger R_1 , and

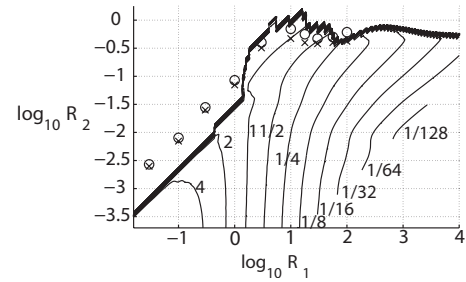


FIG. 3. Contours of the real part of the eigenfrequencies for the most unstable mode in R_1 - R_2 space.

approximately a factor of 3 difference at smaller R_1 . This difference can be attributed mainly to δ -smoothing on the free vortex sheet used in Ref. 8, as explained in Sec. V. We note also that L was erroneously reported as the full flag length in Ref. 8, but it was actually the half-length of the flag in that study (as it is in the present work). By correcting this error in Ref. 8, we also find significantly better agreement with data reported recently by Eloy *et al.*,¹⁸ and with earlier models.^{5,6}

The shape of the stability boundary indicates that lighter flags are generally more stable than heavier flags. We now consider the growth rates within the region of instability which show that this need not be the case. In fact, for a given flag bending modulus, the maximum growth rate occurs at a finite flag mass, not far above the threshold flag mass for instability. Within the instability region we have plotted, we find that fastest growing mode (the mode with the most negative imaginary part) is always the same—the continuation of the first, or lowest-frequency, conjugate pair of eigenmodes of the cantilever. In Fig. 2, we plot the contours of the imaginary part of the eigenvalue for this mode. We find the growth rate increases with decreasing R_2 (which agrees with initial value problem simulations⁸). However, the dependence on flag mass, R_1 , is less intuitive. For R_2 fixed, and below the maximum value for instability to occur (approximately $R_2 = 0.5$), we consider how the growth varies as R_1 goes from small to large. For very small R_1 , the flag is stable. At a threshold $R_1 \sim R_2$, the flag crosses the stability boundary, and the growth rate then increases sharply up to a maximum, which occurs ~ 1 decade in R_1 beyond the stability boundary. Then the growth rate drops by approximately a factor of 4 for each decade in R_1 . Hence there is an optimal flag mass for instability.

We turn now to the real part of the eigenmodes, which correspond to the frequency of oscillation. In Fig. 3 we plot the real part of the eigenmodes only within the region of instability of Fig. 2. For reference we plot also the stability boundary of Fig. 2 (zigzag line). For the cantilever, Eq. (17) shows that the frequency scales as $\sqrt{R_2/R_1}$. In this case the contours of constant frequency are lines where $R_2 \propto R_1$, which is the slope of the contours in the upper right portion of the figure (toward the cantilever limit). At smaller R_1 , the contours have a more vertical slope, so that the oscillation frequency is less sensitive to flag rigidity, and is higher than if it had followed the cantilever behavior.

We have so far considered only the eigenfrequencies of

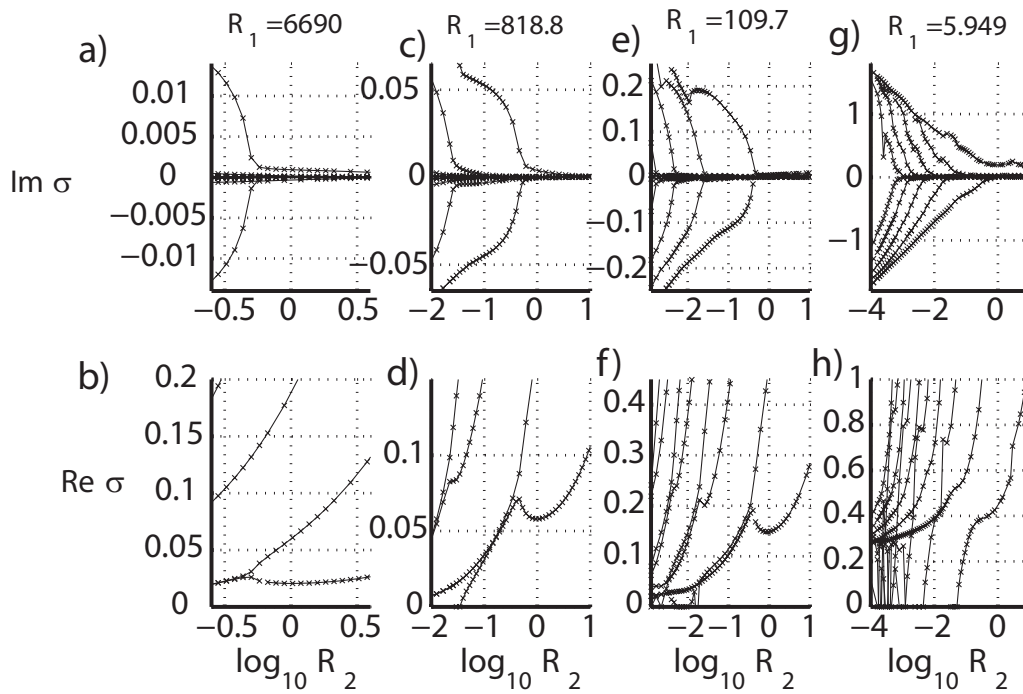


FIG. 4. For four values of R_1 , the real and imaginary parts of the ten eigenfrequencies with smallest real part, vs R_2 .

the first and most unstable eigenmode. As we move toward smaller R_2 , previous experiments¹⁹ and simulations^{8,20} have shown that higher wave number flapping modes appear. Therefore we now consider the instability of higher wave number modes in our model. We fix four values of R_1 , roughly a decade apart, and vary R_2 , tracking the real and imaginary parts of the first ten eigenfrequencies. Figure 4 shows the results. At the highest mass ($R_1=6690$), the two eigenfrequencies with smallest real part [Fig. 4(b)] combine into a conjugate pair of eigenfrequencies near $R_2=10^{-0.3}$. This combination coincides with a bifurcation of the imaginary parts of the eigenmodes away from zero, which yields the instability of the first mode. At the smaller mass $R_1=818.8$ [Figs. 4(c) and 4(d)], we see a similar bifurcation for the first two pairs of modes. The first pair of eigenfrequencies diverges from the conjugate relationship near $R_2=10^{-1}$. This divergence can be seen in the first two eigenmode pairs, of the first four eigenmode pairs which bifurcate at $R_1=109.7$ [Figs. 4(e) and 4(f)]. At the smallest mass shown, $R_1=5.949$ [Figs. 4(g) and 4(h)], we see the bifurcations of the first five pairs of modes. The shape of the curves near the bifurcations is significantly altered from the previous panels, and the eigenfrequencies increase significantly more rapidly with decreasing R_2 . A possible reason for the divergence of the modes from conjugacy is the increase in magnitude of the eigenfrequencies. When $|\sigma| \ll 1$, the linear eigenvalue terms $i\sigma$ are dominant over the nonlinear terms ($-\sigma^2, e^{i\sigma}$) in Eq. (18). Conjugate solutions occur in the linear eigenvalue problem, since for a given eigenfrequency-eigenmode pair $\{\sigma, v\}$, another solution is $\{\bar{\sigma}, \bar{v}\}$. The same is not true when the nonlinear terms are included.

It is important to note that the bifurcation locations in Fig. 4 approximate, but do not precisely coincide with, the loss of stability in R_1 - R_2 space. The stability boundary is

defined as the curve on which the imaginary parts of the eigenvalues are zero. In Fig. 4(a), however, the negative bifurcating curve becomes slightly negative at R_2 somewhat larger than the bifurcation $R_2=10^{-0.3}$. In addition to the stability boundary, it is therefore of interest to delineate separately the bifurcation boundary. For the four values of R_1 in Fig. 4, the bifurcations are defined as the maximum value of R_2 at which the imaginary part of the eigenfrequency has a local maximum in curvature. This corresponds to the kinks in the curves where the bifurcations occur in Fig. 4. We have thus determined the locations of the bifurcation curves for each of the first five bifurcating pairs of eigenfrequencies, over a wide range of R_1 - R_2 space. These are shown in Fig. 5. The number of the bifurcating pair is labeled by k in the figure. For $k=1$, the bifurcation curve is close to the stability boundary of Fig. 2. Subsequent bifurcation curves have a similar transition from flat slope to an approximately power-law increase as R_1 decreases. The power laws apparently

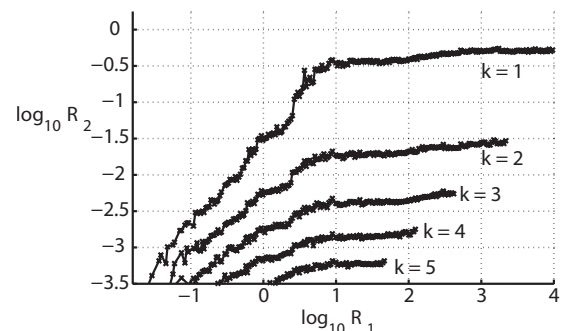


FIG. 5. Bifurcation lines for the first five modes of the flag in R_1 - R_2 . Given k and given R_1 , the value of R_2 corresponds to the location of maximum curvature in the lines in Fig. 4 and corresponding plots for the full range of R_1 shown here.

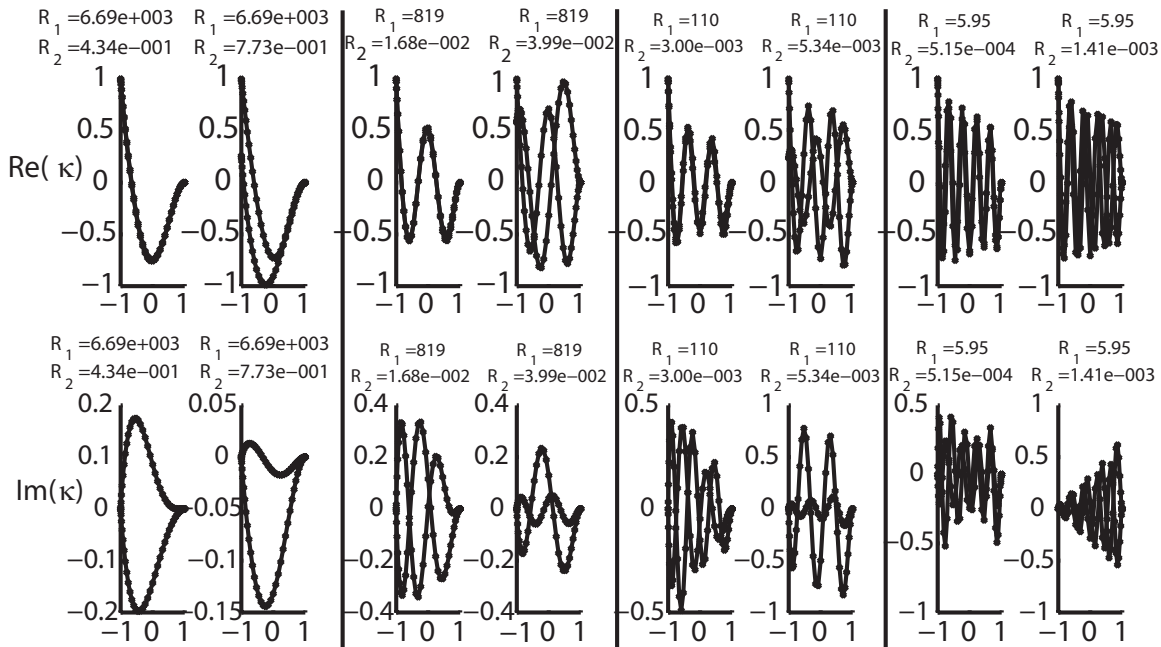


FIG. 6. Corresponding to the eigenfrequency plots of Fig. 4, pairs of eigenmodes. The top row shows the real part and the bottom row shows the imaginary parts of the eigenmode pairs. Moving left to right are four couples (eight columns in all) of plots showing the first four eigenmode pairs at values of R_2 after (left member of couple) and before (right member of couple) the bifurcations shown in Fig. 4.

decrease with increasing k . The curves also become closer, though it is unclear whether for a given R_1 they converge or cross at a finite R_2 , as $k \rightarrow \infty$. As stated previously, the unstable mode of the $k=1$ pair has the fastest growth rate over the full region of R_1 - R_2 space studied here. However, for an infinite flag model introduced by Shelley *et al.*,⁵ we show in Sec. VI that the growth rates of higher wave modes eventually (at sufficiently small R_2) surpass those of all modes with lower wave numbers. When the amplitude of the modes becomes large enough, we approach the nonlinear flag flapping problem studied in Ref. 8. There it was found that the flapping modes become more complex as R_2 decreases in a series of apparently discrete jumps superposed on a background of continuous change in the flapping frequency spectrum. The increasing number of unstable linear modes may contribute to the complexity of the flapping shape when the amplitude enters the nonlinear regime. This point is investigated further in Sec. IV.

Having considered just the 20 lowest modes in this work, we have shown that the flapping instability begins with lowest wave number modes within 3.5 decades of the stability boundary. Furthermore, the growth rate is highest for the lowest wave number modes. Therefore it is reasonable to focus on the lowest wave number modes within the finite range of the stability boundary we consider here.

We have so far considered mainly the changes in eigenfrequency in R_1 - R_2 space. We now consider the corresponding changes in eigenmodes. We begin by examining the changes in eigenmodes when the eigenfrequency passes through the bifurcations just studied. In Fig. 6 we choose the same four values of R_1 as in Fig. 4. For each R_1 , we focus on the bifurcation of just one eigenmode pair, increasing in k as R_1 decreases: $\{k=1, R_1=6690\}$, $\{k=2, R_1=819\}$, $\{k=3, R_1=110\}$, and $\{k=5, R_1=5.95\}$. For each of the four sets $\{k, R_1\}$,

we choose two values of R_2 : one just below the bifurcation for that k (where one of the conjugate eigenfrequencies is unstable), and one just above. The eight panels of Fig. 6 then consist of the two R_2 side by side, for each of the four sets $\{k, R_1\}$. The top row of the eight panels shows the real part of the eigenmode's curvature $\kappa = d^2Y/dx^2$, and the bottom row shows its imaginary part (with amplitude normalized so the real part has value one at $x=-1$). The first of the eight panels shows the $k=1$ mode just beyond the bifurcation. We see that it is approximately a complex-conjugate pair, as we hypothesized in the discussion of Fig. 4. At R_2 above the bifurcation, the modes are clearly not conjugate, but show some resemblances to the conjugate modes. The $k=2-4$ pairs also have the approximately conjugate relationship beyond bifurcation, though the mirror symmetry of the $\text{Im}(\kappa)$ components degrades somewhat with increasing k , in part because the eigenfrequencies are larger in these cases, which moves away from the linear regime where conjugate solutions exist. We see also that the number of peaks increases by one with each k , and that the distribution of curvatures takes a somewhat simple form with monotonic decrease in the peaks in the real parts of the bifurcated eigenmodes, while the prebifurcated modes have less regular distributions of curvature.

We now examine transitions in eigenmodes in a different framework. We return to the stability diagram and growth rate contour plot of Fig. 2, and consider the changes in the first eigenmode corresponding to these changes in frequency. In Fig. 7, the eigenmodes are superposed on the contour plot of Fig. 2. The modes are given a common scale to prevent overlapping, and are located with their horizontal midpoint at the corresponding value of R_1 and their leading edge at the corresponding value of R_2 . The real parts of the modes in Fig. 7(a) appear to undergo a significant change near the

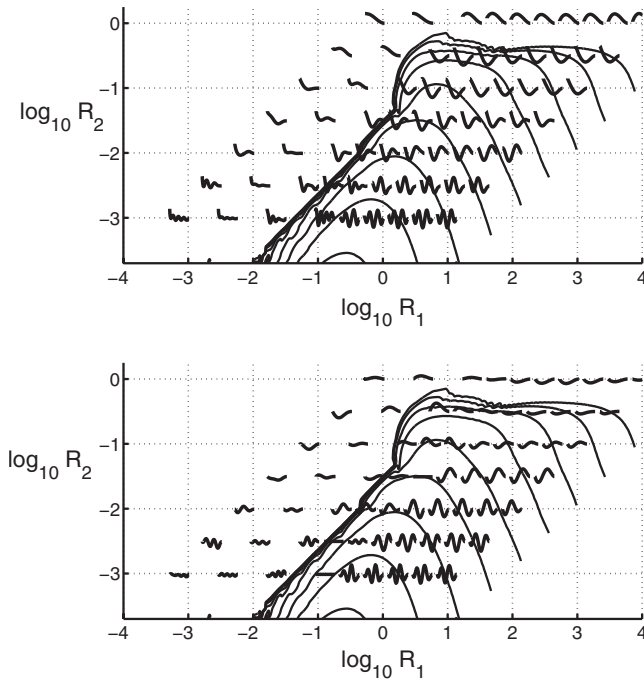


FIG. 7. The shapes $[Y(x)]$ of the first (and most unstable) eigenmode as a function of R_1 and R_2 . The top panel shows the real part of $Y(x)$ and the bottom panel shows the imaginary part. Each shape $Y(x)$ is divided by the maximum of $|Y(x)|$ over x and then scaled by a common value to fit within the plot. Each shape is located with the corresponding value of R_1 at its horizontal midpoint, and the value of R_2 at its leading edge. The shapes are superposed on the contour plot of imaginary parts of the eigenvalues (Fig. 2).

stability boundary—from the first to the second row of shapes, and between the second and third diagonals starting from the left. The latter change is due in part to the sharp gradient in eigenfrequency along the diagonal part of the stability boundary. We note an important change in the eigenvalue problem across the stability boundary—the strength of the free vortex wake changes from exponential decay to exponential growth with distance downstream in the wake. The reason is that trailing-edge vorticity decays exponentially in time for a stable flag. Thus successively generated portions of the wake will have progressively smaller strength, so that the downstream portions of the wake will be relatively stronger. Hence changes in eigenvalues can have a stronger effect in the stable regime, because the wake is stronger. Despite this source of sensitivity, many of the eigenmode shapes in the stable regime are quite similar, particularly at small R_1 and small R_2 , and at large R_1 and large R_2 (where the imaginary part is nearly zero in magnitude). The sharp jump in mode between the first two rows does not obviously correspond to a large change in the imaginary part of the eigenfrequencies (Fig. 2), however. The modes generally obey the cantilever-mode behavior of increasing wave number as R_2 decreases, though mainly in the unstable regime.

We examine the same transitions for the second unstable eigenmode ($k=2$), in Fig. 8. Here we have superposed modes shapes on the bifurcation curves of Fig. 5. We find that at larger R_1 , the real and imaginary parts of the modes are nearly unchanged as R_2 crosses the $k=1$ line, and change

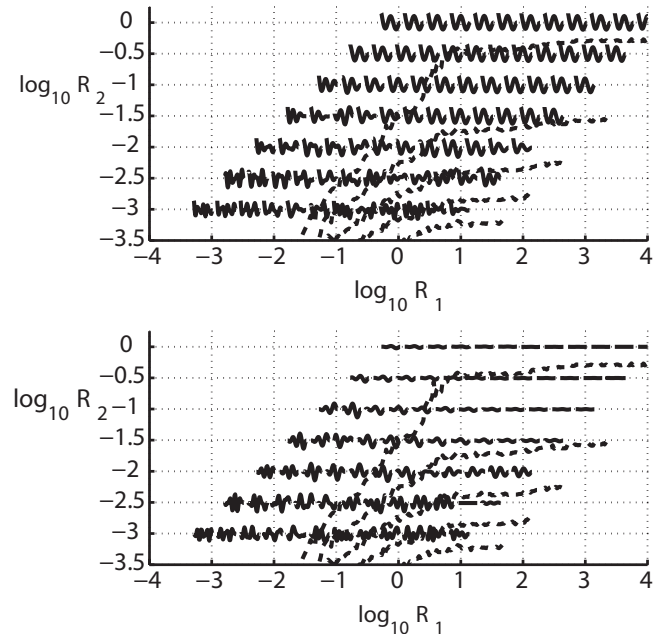


FIG. 8. The shapes $[Y(x)]$ of the fourth eigenmode as a function of R_1 and R_2 . See the caption for Fig. 7 for plotting details. The shapes are superposed on the contour plot of bifurcation lines of the first five eigenmodes (Fig. 5).

rapidly when the $k=2$ line is crossed. This is near where this particular mode becomes unstable, and its vortex wake consequently undergoes a large-amplitude change. Both this mode and the first mode, examined in Fig. 7, have relatively small imaginary part above the flat part of the bifurcation curve (or for the first mode, stability boundary). This behavior may correspond to subdominance of the imaginary part of the equations, which arises from fluid forcing.

IV. COMPARISON WITH LARGE-AMPLITUDE FLAPPING

We now consider the flag flapping instability as an initial value problem rather than the eigenvalue problem studied so far in this work. The initial value problem was studied previously in Ref. 8, which focused on large-amplitude dynamics. Here we consider also the initial value problem in the linear, or small-amplitude regime. We investigate the connection between the dominant mode in the linear regime, and the subsequent large-amplitude dynamics. The problem in the linear regime has two main differences with the eigenvalue problem we have considered so far: the finite length L_w of the free vortex sheet in the eigenvalue problem versus the growing vortex sheet in the initial value problem; and the presence of δ smoothing on the free vortex sheet in the initial value problem,^{8,21,22} which is absent in the eigenvalue problem we have discussed so far. We shall consider the effect of varying these two parameters, δ and L_w , in Sec. V.

We first compute the dynamics of the initial value problem for the flapping flag, after applying a very small perturbation [$O(10^{-5})$ in vertical amplitude at the leading edge over the first unit of dimensionless time (L/U). The flapping amplitude subsequently grows exponentially in time within the unstable regime of R_1 - R_2 space below the crosses in Fig. 2. While growing in amplitude, the flag takes on a single,

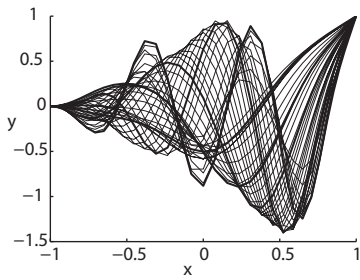


FIG. 9. The eigenmodes in the linear growth regime from an initial value problem simulation with $\delta=0.2$ (Ref. 8), for $R_1=0.1$ and R_2 ranging from 3×10^{-4} to 1×10^{-2} . The wavelength increases with increasing R_2 . The shapes are scaled to have a common deflection at the trailing edge. For five shapes (thicker lines), the first moment of the Chebyshev component amplitudes, a measure of the wave number, are boxed in Fig. 10.

periodically varying shape which we identify as the real part of the dominant eigenmode. We fix a single value of $R_1=0.1$, and decrease R_2 over a factor of 30 moving from the stability boundary into the region of instability, and track the dominant eigenmode. In Fig. 9 we plot the eigenmode when its trailing-edge deflection attains a local maximum in time. We find that the wave number increases as R_2 decreases. The rate of increase is not uniform with respect to R_2 , however. The wave number increases more rapidly in a series of R_2 locations, between which the change is less rapid. In these slowly changing regions, a particular mode appears to be dominant. Hence the change in eigenmode is a continuous increase in wave number, but shows a signature of the discrete series of unstable modes from the eigenvalue problem. We have plotted five of the shapes in Fig. 9 with somewhat darker lines. These shapes correspond to the discrete plateaus in wave number.

The change of wave number is quantified in Fig. 10(a), where we plot the first moment of the Chebyshev component amplitudes of the eigenmodes of Fig. 9 with respect to R_2 . The first moment corresponds roughly to the most dominant wave number. At the upper end of the R_2 range in Fig. 10(a), several modes have nearly the same first moment, up to the first boxed value. In Fig. 9 these modes can be seen clustered around the lowest wave number bold shape, which corre-

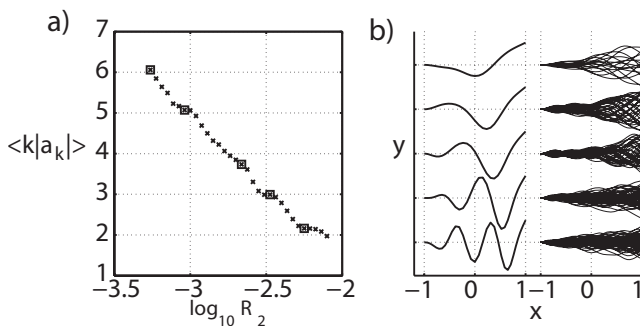


FIG. 10. (a) The first moment of the Chebyshev component amplitudes $|a_k|$ for the eigenmodes in Fig. 9, given by $\langle k|a_k| \rangle = \sum k|a_k| / \sum |a_k|$. The values covered with boxes are highlighted in Fig. 9. (b) For the five eigenmodes in Fig. 9, plotted here on the left, the subsequent large-amplitude dynamics—snapshots over many periods of flapping—plotted on the right.

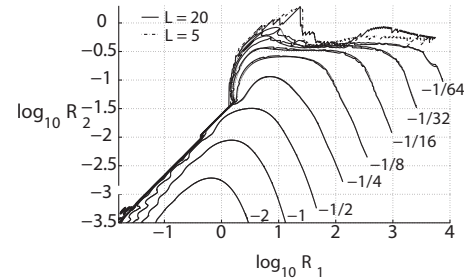


FIG. 11. The same growth rate contours plotted in Fig. 2 (where $L_w=10$), for two different values of wake length: $L_w=5$ and 20.

sponds to the box at largest R_2 in Fig. 10(a). The extent of the plateaus in Fig. 10(a) appears to decrease with each subsequent plateau.

We next consider the relationship between the dominant eigenmode in the linear regime and the subsequent large-amplitude flag dynamics. In Fig. 10(b), we plot on the left the five bold shapes of Fig. 9. To the right of each shape is shown a series of snapshots of the flag dynamics when the amplitude growth has saturated at large amplitude. First, by noting the position of the first minimum in flag deflection in the snapshot envelopes, moving away from the leading edge, we see that the wave number of the large-amplitude shapes increases with the wave number of the linear modes. In addition, the snapshots of the first two shapes correspond to flapping predominantly at a single definite frequency, as was found in Ref. 8. For the third and fourth shapes, there are multiple dominant frequencies, and the fifth shape shows a broad spectrum of frequencies. We have seen in Fig. 5 that increasing numbers of eigenmodes become unstable as R_2 decreases. We may hypothesize that the interaction of multiple unstable modes contributes to the increasing temporal complexity of modes as R_2 decreases.

V. DEPENDENCE ON WAKE LENGTH AND SMOOTHING

In this work we have studied the flapping modes of a flag with a trailing vortex wake of length $L_w=10$, equal to five flag lengths. We consider the effect of varying this important numerical parameter on the stability diagram in Fig. 2. From the Birkhoff–Rott equation¹⁶ and Eq. (4), the effect of vorticity on velocity at point distance d away decays as $1/d$. The integral over a wake of vorticity of alternating sign, with constant strength [$\text{Im}(\sigma)=0$] therefore may be expected to decay as $1/L_w$, by comparing with alternating series which bound the integral from above and below. When the flag is unstable [$\text{Im}(\sigma)<0$], the integral instead decays exponentially in L_w like $e^{\text{Im}(\sigma)L_w}$. In Fig. 11, we replot the stability diagram for $L_w=5$ and $L_w=20$. The two are visually indistinguishable some distance from the stability boundary, where the exponential decay makes the contribution of the vortex wake beyond $L_w=5$ negligible. Close to the neutral-stability boundary the deviation becomes more noticeable, but is still reasonably small.

We turn now to the effect of vortex wake smoothing. Such smoothing was necessary to stabilize the dynamical vortex sheet simulations of Refs. 8, 14, 21, and 22. In order

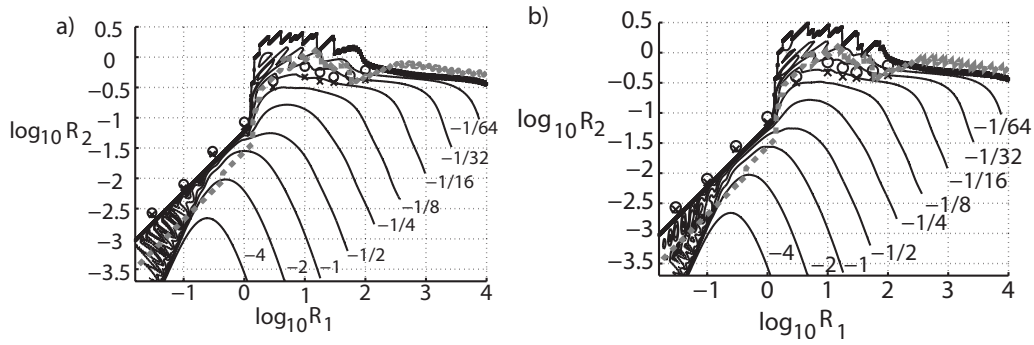


FIG. 12. The stability contours of Fig. 2 for two uniform values of δ on the free sheet: (a) 0.1 and (b) 0.2. The thick gray dashed line shows the stability boundary for $\delta=0$ from Fig. 2.

to compare the stability boundary in this work with the eigenvalue problem, we have recomputed the eigenvalues for a uniform smoothing parameter of $\delta=0.1$ and 0.2 (the value used in Ref. 8). The results with respect to the stability diagram of Fig. 2 are shown in Fig. 12. We find that the nonzero δ move the linearly increasing part of the stability boundary much closer to that computed in Ref. 8. The boundary for $\delta=0.2$ is slightly closer than that for $\delta=0.1$, and both are much closer than that for $\delta=0$ (thick gray dashed line). The upper, relatively flat, portion of the stability boundary moves somewhat further away from that of Ref. 8. One possible reason is the difference between an unsteady simulation with a growing wake and the eigenvalue problem with a wake of fixed length $L_w=10$. Another fact is that the stability boundary position is sensitive to small changes in the imaginary part of the eigenvalues on the upper portion of the stability boundary, where the imaginary part of the eigenvalues have small magnitude over a large region of R_1 - R_2 space.

Aside from the stability boundary, the other contours for $\text{Im}(\sigma)$ are qualitatively similar to the $\delta=0$ case of Fig. 2. However, there is a new region of unstable eigenmodes with small-magnitude imaginary part separating the -4 and -2 contours from the stability boundary.

VI. COMPARISON WITH INFINITE FLAG MODEL

In Ref. 5, Shelley *et al.* studied the linear stability problem for an infinite flag. Although the flag is infinite and has no intrinsic length scale, we follow Ref. 5 and identify a length scale L as that of the finite flag we wish to model with the infinite flag. Using the same dimensionless parameters R_1 and R_2 , based on L , for the infinite flag, Eqs. (1), (3), and (4) become

$$R_1 \partial_{tt} y = -R_2 \partial_{xxxx} y - [p], \quad (19)$$

$$\partial_t y + \partial_x y = \frac{1}{2\pi} \int_{-\infty}^{\infty} \frac{\gamma(x', t)}{x - x'} dx', \quad (20)$$

$$\partial_t \gamma + \partial_x \gamma = \partial_x [p], \quad (21)$$

which are satisfied by the generic solution

$$[y, \gamma, [p]] = [y_0, \gamma_0, [p]_0] \exp[i(\omega t + kx)], \quad (22)$$

where

$$\omega = \frac{-k}{1 + (1/2)R_1|k|} \left[1 \pm \frac{1}{2} |k|^{1/2} d_k^{1/2} \right], \quad (23)$$

$$d_k = R_1 R_2 |k|^3 + 2R_2 |k|^2 - 2R_1. \quad (24)$$

There are two frequencies ω for each k . When d_k is negative the two frequencies are a conjugate pair, with corresponding stable and unstable modes. When d_k is non-negative all modes are neutral.

In Fig. 13 we plot the stability boundary and growth rate contours for the case $k=2\pi$, which is a mode with wavelength equal to the flag length. This is a reasonable approximation to the shape of the fastest growing mode shown in Fig. 6(a). The downward shape of the growth rate contours resembles those of the Fig. 2. The deviation in the location of the stability boundary in the two cases shows the effect of including the free vortex wake, of the assumption that $k=2\pi$, and the fact that L is the half-length of the finite flag and the full length of the flag we are modeling with the infinite flag. The stability boundary in Fig. 13 is given by $R_2 = 2R_1 / (R_1 |k|^3 + 2|k|^2)$. It behaves like $R_1 / |k|^2$ for R_1 small and $2/|k|^3$ for R_1 large. Thus a doubling of k decreases the stability boundary by factors of 4 and 8 in the two regimes. This shift of the stability boundary downward and to the right at larger k agrees with Fig. 5.

We now ask, for which set of parameters is the flag most unstable? The imaginary part of ω is most negative when $R_1 = 2/|k|, R_2 = 0$. Here the stabilizing flag rigidity is zero,

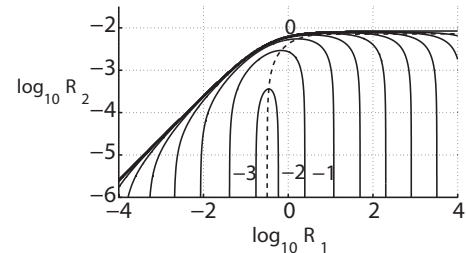


FIG. 13. Stability boundary (marked "0") and growth rate contours for the infinite flag solution with $k=2\pi$. The values of R_1 with maximum growth rate for a given R_2 is shown as a dashed line, and reaches growth rate π in the limit $R_2 \rightarrow 0$. The contours with growth rates 3, 2, and 1 are labeled (by the imaginary part of the eigenvalue, the negative of the growth rate, in correspondence with Fig. 2), and subsequent contours decrease in growth rate by a factor of 2 per contour.

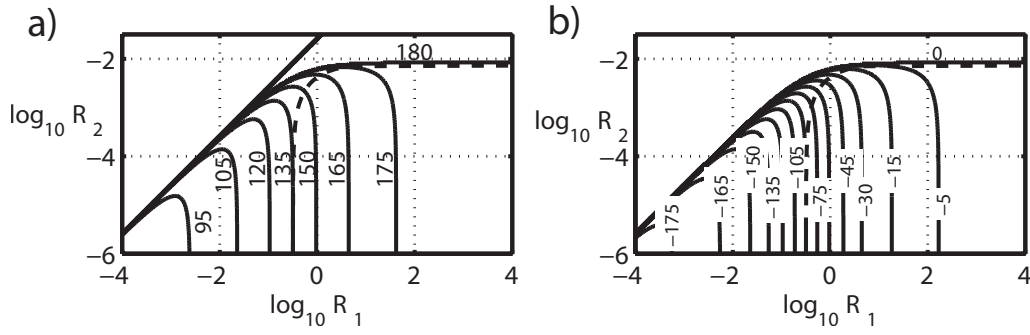


FIG. 14. For the infinite flag solution with $k=2\pi$, the phase difference, in degrees, between the vortex sheet strength γ_0 and flag amplitude y_0 (left), and the pressure jump across the flag $[p]_0$ and flag amplitude y_0 (right). The diagonal line extending upward from the stability boundary on the left marks the line $\omega=-k$, so that growth rate changes from positive to negative, and the phase jumps from 0 to π .

while the flag mass has an intermediate value. At this parameter set, the growth rate of the instability is $|k|/2$, maximum for short wavelengths. However, long-wavelength flags become unstable first, so it is only in the limit $R_2 \rightarrow 0$ that short wavelength flags are the most unstable. The maximum growth rate in Fig. 13 is π , and decays like $1/\sqrt{R_1}$ away from the R_1 for maximum growth rate.

We next consider the physical mechanisms of the flag flapping instability. We begin by writing the quadratic equation for the eigenfrequency ω [from Eq. (19)]:

$$\left(-R_1 - \frac{2}{|k|}\right)\omega^2 + 4 \operatorname{sgn}(k)\omega + R_2 k^4 - 2|k| = 0. \quad (25)$$

Here the inertia and bending rigidity terms are those with factors of R_1 and R_2 , respectively, and the pressure accounts for the remaining terms. The term $-2/|k|$ which multiplies ω^2 is the acceleration part of the pressure force, and gives the additional inertia provided by the fluid (the added-mass effect). We see that the optimal R_1 for instability from the previous paragraph corresponds to the equality of flag inertia and added mass from the fluid in Eq. (25). The term $-2|k|$ acts against the rigidity $R_2 k^4$ of the flag. This is a destabilizing term corresponding to the pressure low at the peaks of a sinusoidal surface with wave number k placed in a steady flow. The role of the linear term $4 \operatorname{sgn}(k)\omega$ is seen more clearly by writing the complex eigenfrequencies ω as

$$\omega = -\frac{B}{2A} \pm \sqrt{\left(\frac{B}{2A}\right)^2 - \frac{C}{A}}, \quad (26)$$

$$\left(\frac{B}{2A}\right)^2 = \left(\frac{4}{2R_1 + 4|k|}\right)^2, \quad (27)$$

$$\frac{C}{A} = \frac{R_2 k^4 - 2|k|}{-R_1 - 2|k|}, \quad (28)$$

where we have explicitly written out the two terms of the discriminant. When negative, their difference corresponds to the square root of the growth rate of the unstable mode. First, we see that for very large flag mass, both terms decay like $1/R_1$, so the growth rate decays like $1/\sqrt{R_1}$. The term $(B/2A)^2$, which gives the contribution of the linear term $4 \operatorname{sgn}(k)\omega$ to stability, is always positive and thus it is stabi-

lizing. The discriminant can be negative only when the second term C/A is larger and thus destabilizing. Since the denominator $A = -R_1 - 2|k|$ is always negative, the numerator must also be negative for instability. It is most negative when the flag rigidity R_2 is zero and k is large.

The foregoing discussion suggests that the mechanism for flag flapping is the competition between the destabilizing pressure low of the steady flow over a wavy surface versus the stabilizing flag rigidity and additional stabilizing fluid term, with all three terms divided by inertia. However, this interpretation is problematic, because when the flag is unstable, it moves in such a way as to shift the pressure lows away from the bumps. This phase difference can be written explicitly in terms of the generic solution (22):

$$\gamma_0 = -2 \operatorname{sgn}(k)(\omega + k)y_0, \quad (29)$$

$$[p]_0 = -2 \frac{(\omega + k)^2}{|k|} y_0.$$

When ω is real (the flag modes are neutrally stable), the flag surface moves with wave speed $-\omega/k$. We see that the vortex sheet strength and pressure jump are proportional to flag amplitude and factors of the relative difference between the flag wave speed $-\omega/k$ and the dimensionless background flow speed 1. Making the Galilean transformation to the rest frame of the flag, we have a steady flow of speed $(1 + \omega/k)$ over a wavy surface, and the pressure lows occur over the bumps.

For unstable waves, the wave speed is

$$-\frac{\operatorname{Re}(\omega)}{k} = \frac{B}{2Ak} = \frac{4}{2R_1 k + 4 \operatorname{sgn}(k)} \quad (30)$$

from Eq. (26). This quantity has magnitude bounded by 1, so that the traveling waves on an infinite flag always move slower than the fluid stream. As soon as the flag becomes unstable (so that ω has a nonzero imaginary part), Eq. (29) implies a phase shift between the bump amplitudes and the vortex sheet strength and pressure jump. These phase shifts are plotted in Fig. 14 for $k=2\pi$. For the maximum growth

rate (dashed line), the pressure phase shift approaches $-\pi/2$ as R_2 becomes small, so that the pressure lows lie between the bumps and troughs, and the pressure difference is zero at the bumps. Figure 14(b) shows that unstable modes are also possible with the pressure *highs* lying over the bumps (zero phase difference between $[p]_0$ and y_0), which would seem to counteract the instability. We also note that when the flag is unstable, the flow is over a wavy surface with traveling waves of growing amplitude. The exponential growth in amplitude of the bumps alters the relative velocity of the flag and the background flow from the case of neutral-stability waves, and shifts the pressure lows away from the peaks of the bumps. However, it remains unclear, particularly for phase shifts greater than $\pi/2$ in magnitude, why such a pressure distribution should enhance growth of the peaks.

VII. CONCLUSION

A recent experiment¹⁹ has found that different flag flapping modes can appear when flow speed is increased (or dimensionless rigidity reduced). Simulations have shown an apparent transition from flapping with a single dominant frequency to multiple frequencies and a broadband response, typical of chaotic dynamics.^{8,20} As a way of rationalizing the increasing complexity of modes observed in experiment, and the onset of chaotic dynamics in simulation, we have shown here that an increasing number of modes, of increasing wave number, becomes unstable as rigidity is reduced. We have found complex transitions in mode shapes across the stability boundary, and a correlation between the number of unstable modes at small amplitude and the complexity of flapping dynamics at large amplitude. Future work may use these unstable modes to show that their interaction produces the series of transitions leading to chaotic dynamics in large-amplitude flapping.⁸ This will provide a partial answer to the question of precisely what mode of large-amplitude flag flapping we are likely to observe for a given set of physical parameters.

- ¹L. Rayleigh, "On the instability of jets," *Proc. London Math. Soc.* **10**, 4 (1878).
- ²R. L. Bisplinghoff and H. Ashley, *Principles of Aeroelasticity* (Dover, New York, 2002).
- ³A. Kornecki, E. H. Dowell, and J. O'Brien, "On the aeroelastic instability of two-dimensional panels in uniform incompressible flow," *J. Sound Vib.* **47**, 163 (1976).
- ⁴L. Zhu and C. S. Peskin, "Simulation of a flapping flexible filament in a flowing soap film by the immersed boundary method," *J. Comput. Phys.* **179**, 452 (2002).
- ⁵M. Shelley, N. Vandenbergh, and J. Zhang, "Heavy flags undergo spontaneous oscillations in flowing water," *Phys. Rev. Lett.* **94**, 094302 (2005).
- ⁶M. Argentina and L. Mahadevan, *Proc. Natl. Acad. Sci. U.S.A.* **102**, 1829 (2005).
- ⁷C. Eloy, C. Souilliez, and L. Schouveiler, "Flutter of a rectangular plate," *J. Fluids Struct.* **23**, 904 (2007).
- ⁸S. Alben and M. J. Shelley, "Flapping states of a flag in an inviscid fluid: Bistability and the transition to chaos," *Phys. Rev. Lett.* **100**, 074301 (2008).
- ⁹L. Segel, *Mathematics Applied to Continuum Mechanics* (Macmillan, New York, 1977).
- ¹⁰L. Prandtl, *Essentials of Fluid Mechanics* (Blackie, Glasgow, UK, 1960).
- ¹¹N. Didden, "On the formation of vortex rings: Rolling-up and production of circulation," *Z. Angew. Math. Phys.* **30**, 101 (1979).
- ¹²D. I. Pullin and A. E. Perry, "Some flow visualization experiments on the starting vortex," *J. Fluid Mech.* **97**, 239 (1980).
- ¹³M. Nitsche and R. Krasny, "A numerical study of vortex ring formation at the edge of a circular tube," *J. Fluid Mech.* **276**, 139 (1994).
- ¹⁴R. K. Shukla and J. D. Eldredge, "An inviscid model for vortex shedding from a deforming body," *Theor. Comput. Fluid Dyn.* **21**, 343 (2007).
- ¹⁵S. Alben, "Optimal flexibility of a flapping appendage at high Reynolds number," *J. Fluid Mech.* **614**, 355 (2008).
- ¹⁶P. Saffman, *Vortex Dynamics* (Cambridge University Press, Cambridge, 1992).
- ¹⁷N. I. Muskhelishvili, *Singular Integral Equations: Boundary Problems of Function Theory and Their Application to Mathematical Physics* (Noordhoff, New York, 1953).
- ¹⁸C. Eloy, R. Lagrange, C. Souilliez, and L. Schouveiler, "Aeroelastic instability of a flexible plate in a uniform flow," *J. Fluid Mech.* **611**, 97 (2008).
- ¹⁹Y. Watanabe, S. Suzuki, M. Sugihara, and Y. Sueoka, "An experimental study of paper flutter," *J. Fluids Struct.* **16**, 529 (2002).
- ²⁰B. S. H. Connell and D. K. P. Yue, "Flapping dynamics of a flag in a uniform stream," *J. Fluid Mech.* **581**, 33 (2007).
- ²¹R. Krasny, "Desingularization of periodic vortex sheet roll-up," *J. Comput. Phys.* **65**, 292 (1986).
- ²²M. Jones, "The separated flow of an inviscid fluid around a moving flat plate," *J. Fluid Mech.* **496**, 405 (2003).